

LaserSAM: Zero-Shot Change Detection Using Visual Segmentation of Spinning LiDAR

Alexander Krawciw
Robotics Institute
University of Toronto
Toronto, Canada
alec.krawciw@mail.utoronto.ca

Sven Lilge
Robotics Institute
University of Toronto
Toronto, Canada
sven.lilge@utoronto.ca

Timothy D. Barfoot
Robotics Institute
University of Toronto
Toronto, Canada
tim.barfoot@utoronto.ca

Abstract—This paper presents an approach for applying camera perception techniques to spinning LiDAR data. To improve the robustness of long-term change detection from a 3D LiDAR, range and intensity information are rendered into virtual perspectives using a pinhole camera model. Hue-saturation-value image encoding is used to colourize the images by range and near-IR intensity. The LiDAR’s active scene illumination makes it invariant to ambient brightness, which enables night-to-day change detection without additional processing. Using the colourized, perspective range image allows existing foundation models to detect semantic regions. Specifically, the Segment Anything Model detects semantically similar regions in both a previously acquired map and live view from a path-repeating robot. By comparing the masks in both views, changes in the live scan are detected. Results indicate that the Segment Anything Model is capable of accurately capturing the shape of arbitrary changes introduced into scenes. The system achieves an object recall of 82.6% and a precision of 47.0%. Changes can be detected through day-to-night illumination variations reliably. After pixel-level masks are generated, the one-to-one correspondence with 3D points means that the 2D masks can be directly used to recover the 3D location of the changes. Eventually, the detected 3D changes can be avoided by treating them as obstacles in a local motion planner.

Keywords—Change Detection; LiDAR Semantic Segmentation

I. INTRODUCTION

Robust perception remains a central challenge for mobile robots operating in unstructured environments. Unlike autonomous cars, there are no rules of the road and rare classes of obstructions occur with a higher frequency [1]. Occlusion effects caused by vegetation degrade the quality of many detectors trained in structured environments [2]. These factors make it difficult for supervised perception pipelines to accurately identify hazards reliably enough to maintain the aggressive performance of the vehicles. In addition to obstacle detection, off-road vehicles must perform terrain assessment to understand which local paths are feasible to drive [3]. Visual Teach and Repeat (VT&R) [4] provides a practical alternative to terrain assessment. A human operator manually drives a robot along a network of connected paths. While driving, the robot constructs local submaps,

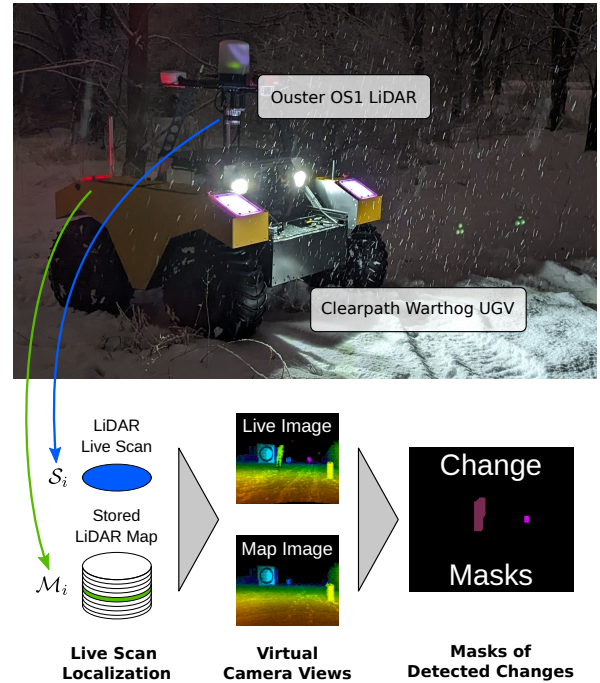


Figure 1. The Clearpath Warthog robot driving at night during snowfall, repeating a path that was previously taught during daytime. This paper proposes LaserSAM to detect and mask environmental changes between teach and repeat paths by creating virtual camera views from LiDAR data and applying modern deep-learning-based segmentations.

which are used later for localization. After the paths are taught, the robot can autonomously navigate between any two locations in the network. The primary responsibility of terrain assessment is delegated to the human pilot, allowing aggressive maneuvers to be demonstrated to the robot. To allow safe repeats over long periods of time, we propose that it is sufficient to detect changes in the scene that intersect the planned local path of the vehicle [5], [6]. During the teach pass, the operator defines a safe corridor [7] around the path. When repeating, the robot navigates around new obstacles within the corridor’s boundary. By focusing on detecting changes instead of specific types of hazards, any type of

obstacle can be detected and avoided without predefining specific classes. For this reason, a robust change-detection module is desired to improve the system’s capabilities.

Existing work on change detection has focused on images from monocular cameras [8] and 3D LiDAR point clouds [9]. Ding et al. [10] use the FastSAM encoder as part of a visual change-detection approach for satellite images. Recently, change detection of point clouds for remote sensing [11] and mobile robotics [12] using deep learning has emerged as an area of study. Conventional cameras have higher resolution than most spinning LiDAR sensors allowing them to detect shapes and textures more accurately. However, the lack of 3D information within the image makes it difficult to accurately transfer 2D segmentations into 3D for path planning [2]. Stereo vision systems can provide 3D information but must solve an additional data association problem. While progress has been made to allow for direct comparison of images through lighting and seasonal changes [13], illumination variation complicates change detection for cameras.

Spinning 360° LiDAR scanners have emerged as a popular, complementary sensor to cameras [14]. LiDAR provides accurate 3D position and intensity measurements for each point. Most automotive LiDAR units operate at a wavelength of 1550 nm because the atmosphere absorbs most of the sun’s energy at that wavelength [15]. Ouster LiDARs operate at 840 nm, which measures significant amounts of ambient light [15]. The combination of ambient and projected infrared light leads to more natural illumination effects that blur the line between passive camera and active LiDAR.

This work blends the strengths of both modalities by rendering perspective camera images from LiDAR scans. This approach allows computer vision algorithms to be applied to multi-view change detection. Specifically, the Segment Anything Model (SAM) [16] and the Fast Segment Anything Model (FastSAM) [17] are used to detect semantic regions in the rendered images. Multi-modal algorithms rely on extrinsic calibration between LiDAR and cameras to define the depth of some pixels in a camera image. In this approach, every pixel in the generated image corresponds exactly to a 3D point. 3D points from the map and the live scan are rendered into a common virtual camera frame for analysis. Finally, the active illumination and signal processing of the 840 nm IR means that change detection works across illumination conditions with no additional processing required. Figure 1 demonstrates the types of conditions that challenge camera-based detection but do not impact the proposed LiDAR pipeline. In summary, we propose the following contribution: a change detection pipeline that leverages the sensor benefits of LiDAR and pre-trained foundation models for image segmentation.

II. RELATED WORK

A. Change Detection

Detecting changes in images, point clouds, or other rich sensors is often a key task in scene understanding [8]. One of the central challenges is to accurately capture the domain-specific semantics. Differentiating inconsequential changes such as illumination and sensor orientation allows for meaningful downstream processing. Ultimately, these definitions must be determined at the problem level but common binary definitions of *changed* and *unchanged* are common in the literature [8]. Most methods operate at the point/pixel level. Aggregation into objects may not be necessary or occur as a downstream processing task.

1) *3D LiDAR Change Detection*: Change detection in point clouds is most commonly applied in remote sensing [9] to detect large-scale changes such as new buildings [11]. Classical methods are usually based on the geometry of the scene. The simplest point-cloud difference evaluates the distance of every point to its nearest neighbour [18] and thresholds distant points as *changed*. These thresholds can be place-dependent [5] to adapt to the local geometry. Alternative approaches use ray-tracing [19] or normal distances [6] to classify points based on fixed or variable thresholds. Deep learning is successful in the change detection of 3D point clouds as well. de Gelis et al. use parallel encoders to train both a supervised [11] and unsupervised [20] neural network that classifies points as added, removed, or the same. These works operate on point cloud maps that are constructed from many different sensor viewpoints, such as the SHREC 2023 dataset [21]. This makes them less applicable to mobile robots, which are heavily affected by occlusions.

2) *2D Camera Change Detection*: Camera change detection can be classified in many ways, but the most relevant detail to this work is whether or not the method assumes a quasi-static background. Quasi-static methods tend to construct a representation of the scene background that is static [22] or adaptive [23]. These methods perform well in video surveillance. Viewpoint variations from mobile robots make them less applicable to the data analyzed here. Fewer methods consider the temporal information from video data and attempt to track changes from a moving camera [24]. This is difficult in the monocular case because the 3D position of the objects is unknown and warping an image into a new frame requires assumptions about the scene or camera motion.

B. Zero-Shot Semantic Segmentation

In 2023, Meta Research released the Segment Anything Model (SAM) [16], which aims to perform semantic segmentation on any type of scene. The model is trained on over eleven million images with more than one billion masks. This vast dataset has enabled the capability to segment regions in a class-agnostic manner. In contrast to common

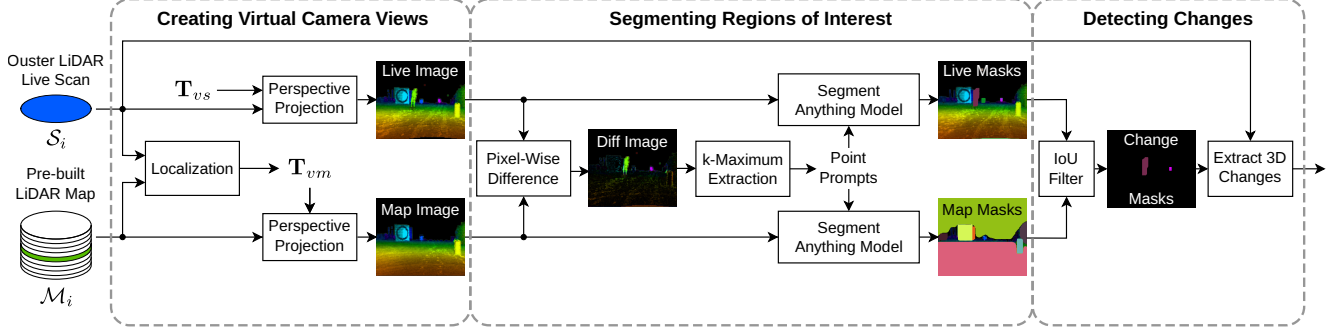


Figure 2. Data processing pipeline of LaserSAM. The pipeline runs for each new frame obtained from the Ouster LiDAR.

datasets for autonomous driving such as CityScapes [25] or SemanticKITTI [26], this allows the model to generate masks on tasks and cameras on which it was not trained. Additionally, the model decoder can accept additional prompts such as points of interest or bounding boxes that refine the masks that are reported. While this performance is impressive, its run time is currently slow for robotics applications.

In response to this runtime constraint, FastSAM [17] was developed based on the YoloV8 [27] architecture. It is trained on the same dataset as Meta’s SAM but the simpler convolutional neural network architecture is much faster than the transformer model used originally. However, the key tradeoff for the speed boost is prompt quality. FastSAM provides a list of masks and confidences but does not consider any additional prompts such as position or bounding boxes. The impacts of this trade-off will be discussed later in the paper.

C. LiDAR as a Camera

The most common LiDAR sensors used in modern autonomous vehicle development are 360° units from Ouster (Velodyne) [28], and RoboSense [29]. These sensors are characterized by higher resolution along the horizontal spinning axis than in the vertical field of view. The current state-of-the-art sensors have 128 vertical beams and operate at 10 to 20 Hz [28]. However, low-framerate LiDAR sensors have existed with much higher resolutions for more than two decades. McManus et al. [30] showed that lighting-invariant visual odometry could be performed using SURF features on intensity images taken from an Autonosys 2D scanning LiDAR. This sensor produces images with a 30°V × 90°H FOV, with resolution 480 × 360 pixels at 2 Hz. The framerate is much slower, but the vertical resolution is still significantly higher (12 pixels per degree) than the OS-1 LiDAR (2.85 pixels per degree) used in this paper. This approach was extended to account for the motion distortion caused by the moving sensor [31] and used to control an offroad vehicle in closed-loop [32], [33].

III. METHOD

This paper ties together past progress in change detection and LiDAR-based image processing with state-of-the-art foundation models. By leveraging the strengths of traditional approaches, and the high-quality segmentation generated by SAM [16], our system can detect previously unseen obstacles, improving the autonomy of a mobile robot.

The proposed change-detection pipeline has three primary stages: creating virtual camera views, segmenting regions of interest, and detecting changes. These stages, as well as the internal steps, are illustrated in Figure 2. The problem inputs are two point clouds: the local submap used in localization M_i and the live LiDAR scan S_i .

A. Creating Virtual Camera Views

The core idea of this pipeline is to project the two aligned point clouds into images, the format expected by SAM. The natural data format of a spinning LiDAR is equirectangular where each pixel corresponds to a constant angular offset. The natural data format of cameras is the perspective projection. Sample images created using both projections are shown in Figure 3. A larger blindspot around the base of the robot is created in the equirectangular view than in the perspective view when deviating from the path (the map view). In the following, we will use the perspective projection because the image segmentation neural networks were trained on data in this form. We define a virtual camera pose in the vehicle’s frame, $T_{cv} \in SE(3)$, which is used to render the images. The desired virtual camera pose is arbitrary, but aligning its position with the origin of the LiDAR sensor minimizes the amount of interpolation required in the final image. The first step is to align the point clouds in the camera frame. When a new live scan is received, an existing ICP-based localization module [34] is used to extract the relative pose of the vehicle in the map ($T_{vm} \in SE(3)$). The extrinsic transformation between the LiDAR sensor and the vehicle, $T_{vs} \in SE(3)$, is known from calibration.

The monocular pinhole camera model [35] is used to render the virtual camera image in the camera frame. By

convention, the z -axis extends forward from the camera. The pixel positions are

$$\begin{bmatrix} u_j \\ v_j \end{bmatrix} = \mathbf{g}(\mathbf{p}_j) = \begin{bmatrix} f_u & 0 & c_u \\ 0 & f_v & c_v \end{bmatrix} \frac{1}{z} \begin{bmatrix} x \\ y \\ z \end{bmatrix}. \quad (1)$$

The image is the union of the intensity values for each pixel in the map point cloud after it is transformed into the camera's frame:

$$I_{\text{map}} = \left\{ \begin{bmatrix} u_j \\ v_j \end{bmatrix} = \mathbf{g}(\mathbf{T}_{cv} \mathbf{T}_{vm_i} \mathbf{p}_{m_i}^j) \mid \mathbf{p}_{m_i}^j \in \mathcal{M}_i \right\}. \quad (2)$$

Similarly, the live scan is

$$I_{\text{live}} = \left\{ \begin{bmatrix} u_j \\ v_j \end{bmatrix} = \mathbf{g}(\mathbf{T}_{cv} \mathbf{T}_{vs} \mathbf{p}_{s_i}^j) \mid \mathbf{p}_{s_i}^j \in \mathcal{S}_i \right\}. \quad (3)$$

The image width (W) and height (H) are set as 256×128 pixels based on the resolution of the OS-1 sensor. Horizontal and vertical fields of view are set to be $\text{fov}_V \times \text{fov}_H = 90^\circ \times 45^\circ$. An ideal, centred camera is used, leading to

$$c_u = W/2, \quad (4a)$$

$$c_v = H/2. \quad (4b)$$

The focal length is defined based on the desired image size and field of view as

$$f_u = \frac{W}{2 \tan(\text{fov}_H/2)}, \quad (5a)$$

$$f_v = \frac{H}{2 \tan(\text{fov}_V/2)}. \quad (5b)$$

Points beyond the field of view are ignored, and if multiple points are captured by the same pixel, the closest point to the camera is retained.

When a perspective projection is used, gaps in the image are created due to the distortion. These gaps are highlighted in the third row of Figure 3. Interpolating these regions is critical for the segmentation to work properly. A 3×3 kernel is used to interpolate the missing pixels, but only non-zero pixels are considered. The distortion is exacerbated by offsetting the virtual camera's origin from the LiDAR. Conceptually, the virtual camera could be colocated with the LiDAR's position in either the teach or repeat. However, we choose to locate it in the repeat frame because the map point clouds are an accumulation of points from sequential scans. The hue-saturation-value colour model is used to colour the images by range. The z coordinate in the camera frame is used for hue, mapping over a maximum range of 50 m. The saturation is the constant 255 for all pixels and the value is the LiDAR intensity of the pixel. The first column of Figure 4 shows two sample images rendered from the robot in a common frame.

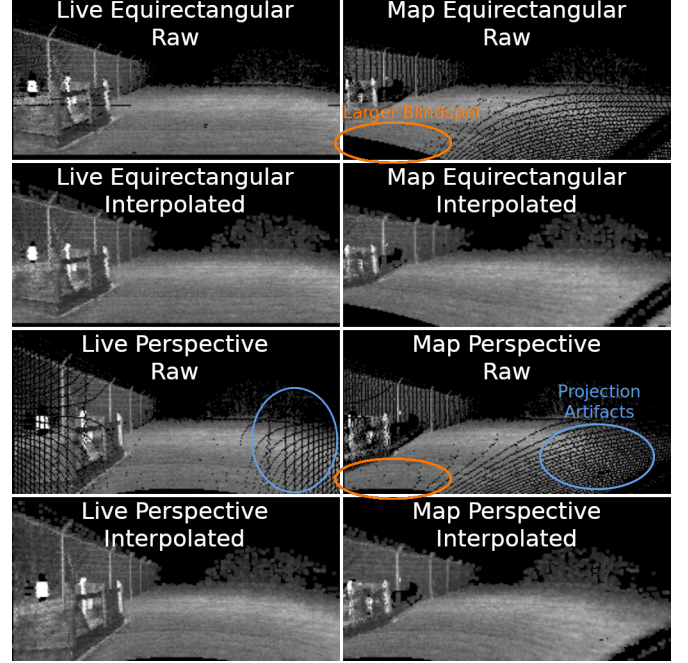


Figure 3. The left column contains equirectangular and perspective images aligned with the LiDAR. The right column shows the two projections with a two-meter lateral offset. The perspective view has a smaller blind spot around the base of the robot.

B. Segmenting Regions of Interest

After rendering both images in a common frame, segmentation occurs. We compare the performance of SAM and FastSAM for this step. SAM can perform segmentation based on point prompts of interest. To generate point prompts, the norm of the pixel-wise difference of the two images is evaluated. The top k local maxima of the resulting 2D surface are used as prompts to the model. The model is prompted twice, once using the live image and once using the map image. This generates two lists, each containing k masks from the live and map images, respectively.

FastSAM cannot accept prompts in the same way as SAM. Instead, the model is evaluated independently for each image. This means that there are two lists of masks at each timestep. The two lists of masks are independent meaning their lengths often differ and a correspondence problem presents itself to associate masks in teach and repeat.

C. Detecting Changes

After independently segmenting the images, the detected masks are compared. To decide if two masks capture the same object, the intersection-over-union (IoU) score is calculated between them. The bitwise AND (\wedge) and OR (\vee) operations are used to calculate the IoU of two binary masks ($b1, b2$),

$$\text{IoU} = \frac{\sum_i \sum_j b1[i][j] \wedge b2[i][j]}{\sum_i \sum_j b1[i][j] \vee b2[i][j]}. \quad (6)$$

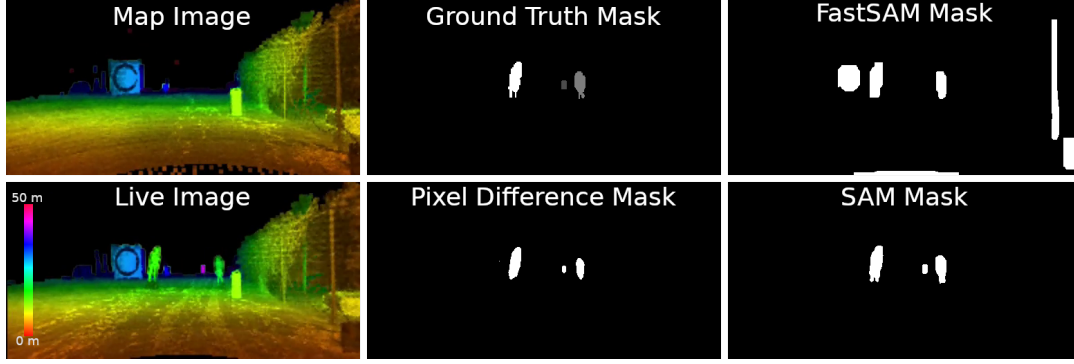


Figure 4. Change-detection masks for a sample frame. The left column shows the input images. There are three changed objects, marked in the ground truth. The segmentation results for each algorithm are shown in their respective panel.

An IoU score of one indicates a perfect match and zero means no overlap between the individual masks. Masks with a maximum IoU of less than 0.5 are considered to be *changed* between the live scan and the map. The remaining masks are considered *unchanged*. For SAM, this is a direct comparison of the matched lists. For FastSAM, a brute-force comparison between every mask in the two scans is required. There are typically fewer than ten masks so this is computationally acceptable. All points classified as *changed* in the live scan are then back-projected into 3D. The 3D bounding box, centroid, or raw points can be estimated and provided to a local planner. A corridor-constrained sampling-based planner [7] inflates the *changed* points to account for the robot’s footprint and avoids them.

IV. EXPERIMENTS

Experiments were performed at the University of Toronto’s Institute for Aerospace Studies using a Clearpath Warthog UGV [36] equipped with an Ouster OS-1 128 beam LiDAR [28]. Data were recorded during night and day as well as during snowstorm conditions. Static obstacles placed on and around the original path and pedestrians walking near the robot were introduced as changes in the dataset. A mixture of natural and fabricated items was used to minimize the impact of the chosen materials’ reflectivity on the experiments. Additionally, duplicate items were placed near the path as part of the static scene. This demonstrates that the algorithm is performing change detection, not obstacle classification. Two different sequences were recorded with changes. The first sequence is 262 m long on relatively flat terrain with cones, mannequins, and road signs as obstacles.

The second sequence is 230 m long through wooded areas with pedestrians and a single cone obstacle. The forest sequence is notable because the teach pass occurred during daylight and the repeat pass was recorded in the dark, about six hours later.

The dataset has 7386 live scans to use for testing. To provide an initial, quantitative evaluation of the change detection quality, 92 frames were manually annotated to provide ground truth masks. The frames were randomly selected, using a sampling bias towards frames containing changes. The ground-truth masks were instance segmented to allow for per-object metrics to be evaluated in addition to per-pixel ones. As discussed in the related work, the precise semantic meaning of a change is problem-dependent. In this dataset, only new or moved obstacles that would impact the robot’s ability to drive were marked as changed. Small scene changes such as footprints in the snow, or tracks from previous drives were marked as *unchanged*. Additionally, we did not segment the teach images to mark areas where an object was removed.

A. Results

The pipeline was evaluated on the annotated subset of the frames. Specifically, SAM and FastSAM were compared to the baseline pixel-wise difference algorithm, which was used to create the point prompts for SAM. Two metrics are used for comparison: the pixel-wise IoU between the predicted and ground-truth segmentation masks and the F-score of objects being detected. The ground truth is instance-segmented, which allows for the evaluation to consider individual changes in the same frame, and whether or not

Table I
COMPARISON OF SAM, FASTSAM, AND PIXEL DIFFERENCE CHANGE DETECTION ALGORITHMS.

	Method	Pixel-Wise IoU	Object Precision	Object Recall	Object F-Score	Run Time (ms)
Baseline	Pixel Difference	20.7%	10.4%	53.0%	17.4%	5.7 ± 1.2
Ours {	FastSAM	12.3%	22.3%	77.4%	34.6%	13.6 ± 2.1
	SAM (sam_vit_b)	25.9%	47.0%	82.6%	59.9%	322 ± 35

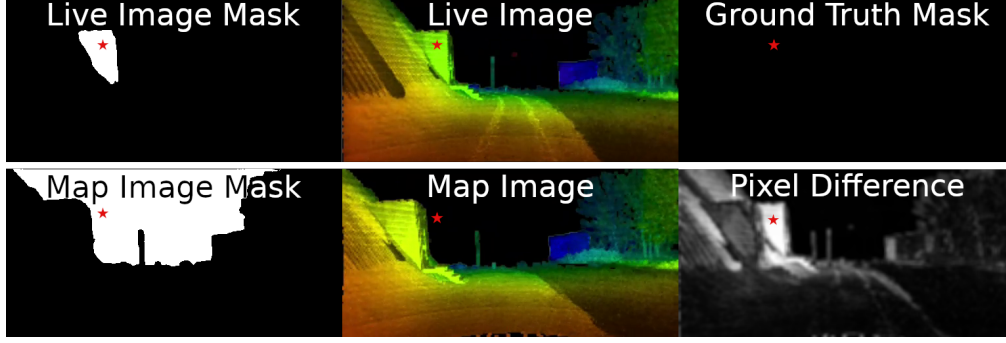


Figure 5. A false positive detection due to misalignment. Localization has an angular error that leads to an inaccurately large pixel difference. The prompt point (red star) exists in a region that crosses the object boundary between the live and map images.

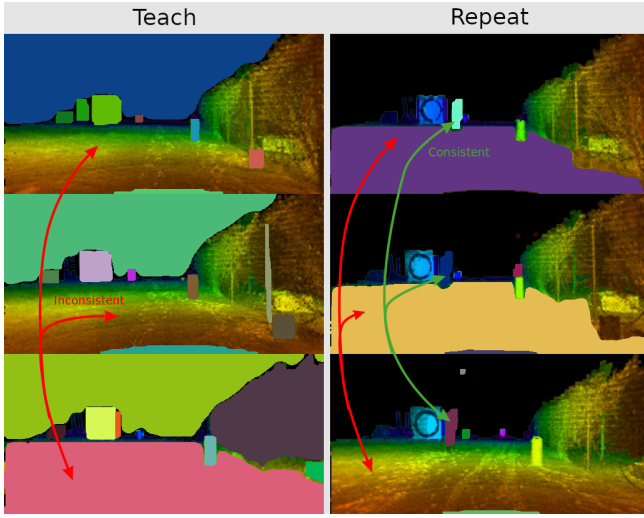


Figure 6. A temporal sequence of the semantic regions generated by FastSAM [17]. The mask colours are randomly generated. The green arrows highlight consistent mask regions through time. Red arrows point to masks that flicker in time, which is a challenge for stable processing.

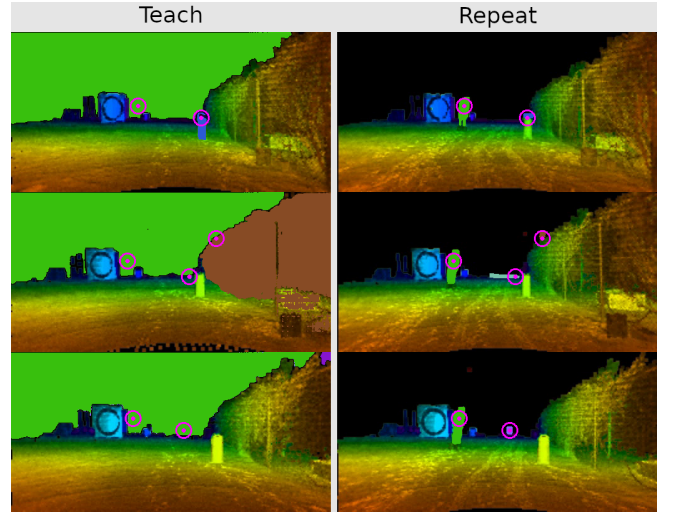


Figure 7. A temporal sequence of semantic regions generated by SAM [16]. The shared prompt point is highlighted in the pink bulls-eye. The mask colours match between the teach and repeat. Prompts often exist near the boundaries, which is undesirable.

they are detected. An overlap of 50% IoU is used as the threshold for a true positive detection for the object-based metrics. After counting the number of true positives (TP), false positives (FP), and false negatives (FN) detections, the precision, recall, and F-score can be evaluated [37]. The achieved results are summarized in Table I. All computational timing was performed on a laptop NVIDIA RTX A4500 GPU.

Figure 4 shows the segmentation result for a sample frame with a moving pedestrian, static cone and static mannequin. All three methods correctly find the three objects but FastSAM marks extra objects, and SAM has the most accurate segmentation boundary. In our experiments, SAM outperforms both other methods by a significant margin.

In its current state, the system has a high recall, but low precision; there are too many false positives. Qualitative analysis provides some additional insight into the results. SAM and FastSAM tend to over-segment in failure cases.

The most commonly observed failure mode during our experiments is a localization error, causing a large difference on the static object region boundary. In Figure 5, live and map images are not prompted inside the same object so SAM segments large, non-overlapping regions. This has an outsized impact on the IoU because many false-positive pixels are added to the IoU calculation. On the object level, the results are more encouraging. In successful frames, such as Figure 7, the changes are captured accurately and there are no isolated bright pixels common in the baseline or 3D point clouds approaches. We anticipate that with improved localization, the number of large, static false-positive detections will fall rapidly.

Figure 6 provides a sample set of three matched teach and repeat frames extracted using FastSAM. Critically, the changed objects are classified correctly within the scene. However, some masks flicker and are not retained as desired. Sometimes the ground is not masked as a region in the teach

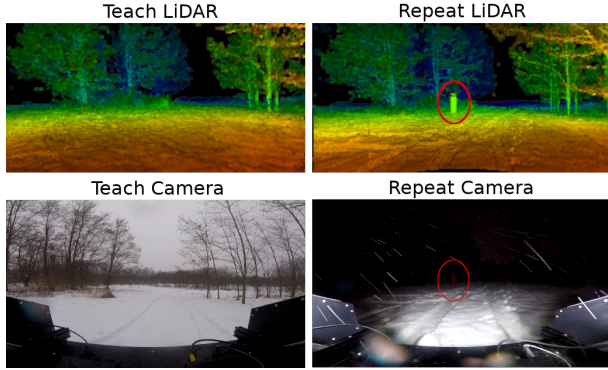


Figure 8. The rendered LiDAR images are not affected by ambient lighting conditions. The teach was performed during sunlight and the repeat was performed in the dark, and during heavier snow.

pass leading to an error where the entire ground may be considered a change in the repeat. While post-processing filters this out based on size, ground errors near the robot have the largest impact on the path planner downstream.

Figure 7 shows an example sequence of masks generated by SAM. When changes are detected, the map image often has a large mask corresponding to the ground or background. Once the two masks are generated, the same IoU threshold comparison is used, as with FastSAM. The masks from SAM tend to be more consistent over time. This is advantageous for robot motion planning.

The ambient illumination of the scene does not affect detection quality. Figure 8 shows the two virtual images in the afternoon and night. The colouring of the images is qualitatively indistinguishable. This is a significant benefit compared to using a conventional camera with the same approach. Qualitatively, it appears that SAM finds accurate segmentation boundaries, which can be challenging near interfaces.

B. Limitations

Existing foundation models are trained on colour RGB images, not greyscale nor HSV range-colourized images. The extracted features are likely less expressive than the network’s capability.

Similar to works that process point clouds directly, occluded regions remain a challenge. Figure 9 highlights two regions that are affected by occlusions. Figure 9 is originally rendered from a different pose than the LiDAR meaning that occluded parts of the scene are visible from the new view. This causes a shadow effect from the structure of the robot’s supports. The further from the LiDAR’s origin that the virtual camera is rendered, the more gaps there are in the visual frame. The submap has fewer occlusion-based gaps because it is constructed from sequential frames. Points within the magenta region of Figure 9 were appended to the local submap during the teaching process, filling in some

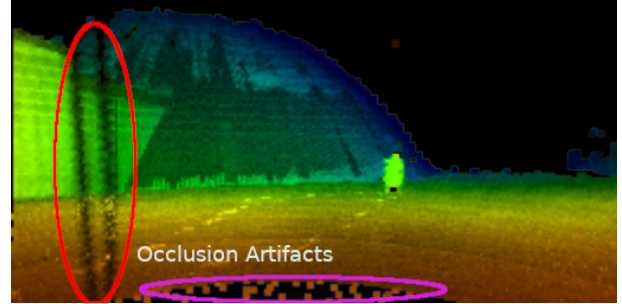


Figure 9. Range-coloured image highlighting the effect of the occlusions and submaps. In the red ellipse, a shadow in the scan is visible from the beam of the robot that blocked the LiDAR in the teach. In the magenta ellipse, points are visible in the local blindspot of the sensor because the submap contains a union of points from multiple scans.

of the holes caused by displacing the virtual camera. If storage was not an issue, retaining every point from nearby teach frames would allow for denser map representations and minimize occlusion effects. In teach and repeat, the robot’s lateral path displacements are typically less than two meters, which minimizes these effects in practice. A final challenge involves the accuracy of the localization algorithm. If the relative transformation between the two point clouds is inaccurate, the rendered images are misaligned and the intersection of the masks check will fail. In the perspective view, small angular misalignments have a large impact on the image location of distant changes. Small translational errors, particularly along the z -axis of the camera, impact the position of nearby changes.

C. Future Work

Currently, the method has only been evaluated on one type of LiDAR sensor. However, it would be interesting to understand how much the intensity quality impacts overall performance. A potential ablation study could add increasing levels of noise to the intensity data, eventually resulting in uniform white noise coloured only by range. To improve temporal consistency and add tracking, the centroid of previous obstacles will be projected into the camera at the next timestep and used as a prompt. Changes will likely remain visible in the scene, so prompting on their estimated location should improve temporal consistency. Inconsistent masks could be filtered out as spurious. Lastly, this work only considers positive changes: items added in the live scan. It should be possible to detect items that existed in the teach pass on the path that were removed. Due to the manual teach process, it is unlikely that the robot will be driven over items that can disappear so this is left for future investigation.

V. CONCLUSION

Robust environmental perception by mobile robots remains an exciting field for further study. This paper demonstrates that further developments in the hardware sensitivity

of LiDAR scanners will enable more algorithms that leverage the benefits of multi-modal detection but use only a single LiDAR sensor. While the resolution of commodity LiDAR-rendered images lags behind conventional cameras, it has reached sufficient thresholds to apply vision algorithms to field robots. It is particularly encouraging that these algorithms naturally work through illumination changes from night to day and day to night. Although the 3.1 Hz Segment Anything Model is slower than the 73 Hz FastSAM, the ability to prompt masks based on the live pixel-level difference in intensity and the previously viewed obstacles makes it more effective than the FastSAM frame-by-frame approach. The classic trade-off between speed and effectiveness leaves both foundation models as viable methods for future evaluation. We look forward to building on these results; implementing the neural network live on the robot and running it in closed-loop with our path planner.

REFERENCES

- [1] Z. Ma, Y. Yang, G. Wang, X. Xu, H. T. Shen, and M. Zhang, "Rethinking Open-World Object Detection in Autonomous Driving Scenarios," in *Proceedings of the 30th ACM International Conf. on Multimedia*, New York, NY, USA, Oct. 2022, pp. 1279–1288.
- [2] R. Qin, J. Tian, and P. Reinartz, "3d change detection – approaches and applications," *ISPRS J. of Photogrammetry and Remote Sensing*, vol. 122, pp. 41–56, 2016.
- [3] P. Papadakis, "Terrain traversability analysis methods for unmanned ground vehicles: A survey," *Engineering Applications of Artificial Intelligence*, vol. 26, no. 4, pp. 1373–1385, 2013.
- [4] P. Furgale and T. D. Barfoot, "Visual teach and repeat for long-range rover autonomy," *J. of Field Robotics*, 2010.
- [5] L.-P. Berczi and T. D. Barfoot, "It's like déjà vu all over again: Learning place-dependent terrain assessment for visual teach and repeat," in *2016 IEEE/RSJ International Conference on Intelligent Robots and Systems (IROS)*, 2016, pp. 3973–3980.
- [6] Y. Wu, "VT&R3: Generalizing the teach and repeat navigation framework," Sep. 2022, mASc Thesis.
- [7] J. Sehn, J. Collier, and T. D. Barfoot, "Off the beaten track: Laterally weighted motion planning for local obstacle avoidance," 2023.
- [8] C. Stauffer and W. Grimson, "Learning patterns of activity using real-time tracking," *IEEE Trans. Pattern Anal. Mach. Intell.*, vol. 22, no. 8, pp. 747–757, 2000.
- [9] U. Okyay, J. Telling, C. L. Glennie, and W. E. Dietrich, "Airborne lidar change detection: An overview of earth sciences applications," *Earth-Science Reviews*, vol. 198, p. 102929, 2019.
- [10] L. Ding, K. Zhu, D. Peng, H. Tang, K. Yang, and B. Lorenzo, "Adapting segment anything model for change detection in hr remote sensing images," *arXiv preprint arXiv:2309.01429*, 2023.
- [11] I. de Gélis, S. Lefèvre, and T. Corpetti, "Siamese KPConv: 3D multiple change detection from raw point clouds using deep learning," *ISPRS J. of Photogrammetry and Remote Sensing*, vol. 197, pp. 274–291, Mar. 2023.
- [12] A. Krawciw, J. Sehn, and T. D. Barfoot, "Change of scenery: Unsupervised lidar change detection for mobile robots," 2023.
- [13] Y. Chen, B. Xu, F. Dömbgen, and T. D. B. Barfoot, "What to learn: Features, image transformations, or both?" in *IEEE/RSJ International Conference on Intelligent Robots and Systems (IROS)*. IEEE, 2023.
- [14] L. Wijayathunga, A. Rassau, and D. Chai, "Challenges and solutions for autonomous ground robot scene understanding and navigation in unstructured outdoor environments: A review," *Applied Sciences*, vol. 13, no. 17, p. 9877, 2023, number: 17 MDPI.
- [15] Ouster. How multi-beam flash lidar works. [Online]. Available: <https://ouster.com/insights/blog/how-multi-beam-flash-lidar-works>
- [16] A. Kirillov, E. Mintun, N. Ravi, H. Mao, C. Rolland, L. Gustafson, T. Xiao, S. Whitehead, A. C. Berg, W.-Y. Lo, P. Dollár, and R. Girshick, "Segment anything," 2023.
- [17] X. Zhao, W. Ding, Y. An, Y. Du, T. Yu, M. Li, M. Tang, and J. Wang, "Fast Segment Anything," 2023.
- [18] D. Girardeau-Montaut, M. Roux, R. Marc, and G. Thibault, "Change detection on points cloud data acquired with a ground laser scanner," *International Archives of Photogrammetry, Remote Sensing and Spatial Information Sciences*, vol. 36, no. 3, p. W19, 2005.
- [19] J. P. Underwood, D. Gillsjö, T. Bailey, and V. Vlaskine, "Explicit 3D change detection using ray-tracing in spherical coordinates," in *2013 IEEE International Conf. on Robotics and Automation*, May 2013, pp. 4735–4741, iISSN: 1050-4729.
- [20] I. de Gélis, S. Saha, M. Shahzad, T. Corpetti, S. Lefèvre, and X. Zhu, "Deep unsupervised learning for 3d als point clouds change detection," *ISPRS Open Journal of Photogrammetry and Remote Sensing*, vol. 9, p. 100044, 08 2023.
- [21] Y. Gao, H. Yuan, T. Ku, R. C. Veltkamp, G. Zamanakos, L. Tsochatzidis, A. Amanatiadis, I. Pratikakis, A. Panou, I. Romanelis, V. Fotis, G. Arvanitis, and K. Moustakas, "SHREC 2023: Point cloud change detection for city scenes," *Computers & Graphics*, vol. 115, pp. 35–42, 2023.
- [22] P.-L. St-Charles, G.-A. Bilodeau, and R. Bergevin, "Subsense: A universal change detection method with local adaptive sensitivity," *IEEE Transactions on Image Processing*, vol. 24, no. 1, pp. 359–373, 2015.
- [23] C. Stauffer and W. Grimson, "Learning patterns of activity using real-time tracking," *IEEE Transactions on Pattern Analysis and Machine Intelligence*, vol. 22, no. 8, pp. 747–757, 2000.
- [24] K. Toyama, J. Krumm, B. Brumitt, and B. Meyers, "Wallflower: principles and practice of background maintenance," in *Proceedings of the Seventh IEEE International Conf. on Computer Vision*, vol. 1, 1999, pp. 255–261 vol.1.
- [25] M. Cordts, M. Omran, S. Ramos, T. Rehfeld, M. Enzweiler, R. Benenson, U. Franke, S. Roth, and B. Schiele, "The cityscapes dataset for semantic urban scene understanding," in *Proc. of the IEEE Conf. on Computer Vision and Pattern Recognition (CVPR)*, 2016.
- [26] J. Behley, M. Garbade, A. Milioto, J. Quenzel, S. Behnke, C. Stachniss, and J. Gall, "SemanticKITTI: A Dataset for Semantic Scene Understanding of LiDAR Sequences," in *Proc. of the IEEE/CVF International Conf. on Computer Vision (ICCV)*, 2019.
- [27] G. Jocher, A. Chaurasia, and J. Qiu. (2023) Ultralytics yolov8. [Online]. Available: <https://github.com/ultralytics/ultralytics>
- [28] "Ouster OS1 LiDAR," Available Online [<https://ouster.com/>]

products/scanning-lidar/os1-sensor/].

- [29] “Robosense LiDAR,” Available Online [https://www.robosense.ai/en].
- [30] C. McManus, P. Furgale, and T. D. Barfoot, “Towards lighting-invariant visual navigation: An appearance-based approach using scanning laser-range finders,” *Robotics and Autonomous Systems*, vol. 61, no. 8, pp. 836–852, 2013.
- [31] S. Anderson and T. D. Barfoot, “Ransac for motion-distorted 3d visual sensors,” in *2013 IEEE/RSJ International Conf. on Intelligent Robots and Systems*. IEEE, 2013, pp. 2093–2099.
- [32] C. McManus, P. Furgale, B. Stenning, and T. D. Barfoot, “Lighting-invariant visual teach and repeat using appearance-based lidar,” *J. of Field Robotics*, vol. 30, no. 2, pp. 254–287, 2013.
- [33] T. D. Barfoot, C. McManus, S. R. Anderson, H. Dong, E. Beerepoot, C. H. Tong, P. T. Furgale, J. D. Gammell, and J. Enright, “Into darkness: Visual navigation based on a lidar-intensity-image pipeline,” in *International Symposium of Robotics Research*, 2013.
- [34] K. Burnett, Y. Wu, D. J. Yoon, A. P. Schoellig, and T. D. Barfoot, “Are We Ready for Radar to Replace Lidar in All-Weather Mapping and Localization?” *IEEE Robotics and Automation Letters*, vol. 7, no. 4, pp. 10 328–10 335, Oct. 2022.
- [35] T. D. Barfoot, *State Estimation for Robotics: Second Edition*, 2nd ed. Cambridge University Press, 2024.
- [36] “Clearpath Robotics Warthog UGV,” 2020. [Online]. Available: <https://clearpathrobotics.com/warthog-unmanned-ground-vehicle-robot/>
- [37] C. J. Van Rijsbergen, “Chapter 7: Evaluation,” in *Information Retrieval*, 2nd ed. Butterworths.